
Jet evolution in a quantum computer: quark and gluon dynamics

N. F. Castro^{a,1,2}, J. G. Milhano^{b,3,4}, M. G. Jordão Oliveira^{c,2,5}

¹Departamento de Física, Escola de Ciências, Universidade do Minho, 4710-057 Braga, Portugal

²LIP – Laboratório de Instrumentação e Física Experimental de Partículas, Escola de Ciências, Campus de Gualtar, Universidade do Minho, 4701-057 Braga, Portugal

³LIP – Laboratório de Instrumentação e Física Experimental de Partículas, Avenida Professor Gama Pinto 2, 1649-003 Lisboa, Portugal

⁴Instituto Superior Técnico, Universidade de Lisboa, Avenida Rovisco Pais 1, 1609-001, Lisboa, Portugal

⁵Present affiliation: NNF Quantum Computing Programme, Niels Bohr Institute, University of Copenhagen, Denmark

February 6, 2025

Abstract The intrinsic quantum nature of jets and the Quark-Gluon Plasma makes the study of jet quenching a promising candidate to benefit from quantum computing power. Standing as a precursor of the full study of this phenomenon, we study the propagation of SU(3) partons in Quark-Gluon Plasma using quantum simulation algorithms. The algorithms are developed in detail, and the propagation of both quarks and gluons is analysed and compared with analytical expectations. The results, obtained with quantum simulators, demonstrate that the algorithm successfully simulates parton propagation, yielding results consistent with analytical baseline calculations.

Keywords Jets · Jet quenching · Quantum computing · Quantum simulation

1 Introduction

Jets, which are highly collimated beams of particles [1], are one of the most common probes used to study the Quark-Gluon Plasma (QGP) produced in ultra-relativistic heavy-ion collisions. Jets originate from the fragmentation of hard partons (quarks or gluons). Despite their complexity, jets are excellent probes because their behaviour in vacuum is understood, offering a baseline for comparison. Furthermore, jet properties are modified due to the interaction with the QGP, a phenomenon commonly referred to as jet quenching (for reviews see [2, 3, 4, 5, 6, 7]). Jet quenching has remained a hot topic throughout the last decades, leading to the development of new techniques to simulate the jet quenching phenomenon and extract QGP properties [8, 9, 10, 11, 12].

Simultaneously, advances in quantum computing have opened new avenues for studying complex systems. Enabled by the advent of intense sources of highly entangled photons [13, 14], through the exploration of inherent properties of quantum mechanics systems, namely superposition, entanglement, and interference, quantum computers are equipped with operations without classical analogs, enabling the treatment of classical hard or even forbidden problems. Despite all the developments and all the groundbreaking claimed advantages, most of the theoretically proved quantum advantages can only be obtained with fault-tolerant devices which are quite different from the currently available Noise Intermediate-Scale Quantum (NISQ) devices [15]. NISQ devices face limitations in qubit count, coherence time, and susceptibility to noise, restricting the practical implementation of quantum algorithms. As a result, the development of quantum software and quantum algorithms is still in a more theoretical stage, with only a few pertinent quantum algorithms being successfully implemented in real quantum devices. So, at present, one may approach the development of quantum algorithms via two main lines of thought: the development of quantum algorithms for the current quantum devices attending to all the limitations and demands, and the development of quantum algorithms for the future fault-tolerant quantum devices without major concerns about the current limitations. Here, with the long-term goal of one day solving the jet quenching problem and noting the the complexity and dimension of the problem, the second line of thought is followed.

While quantum algorithms for jet quenching are still in their infancy, there has been growing interest in applying quantum computing to this problem. As a precursor of the evolution of a jet in quantum chromodynamics medium, an algorithm for the evolution of a hard probe, a quark, in a colour background was proposed in [16]. Later, a simpler variant of this algorithm was implemented on quantum simulators and real quantum devices [17]. This variant was also extended to demonstrate that it can also be used to simulate jet evolution matter. In 2023, these algorithms were further extended to account for gluon production [18], and this complex algorithm was implemented in quantum simulators. Here, we develop and implement new and more complex quantum algorithms for jet quenching, namely for the evolution of both SU(3) quarks and gluons in QGP media.

^ae-mail: nuno.castro@cern.ch

^be-mail: gmilhano@lip.pt

^ce-mail: maria.oliveira@nbi.ku.dk

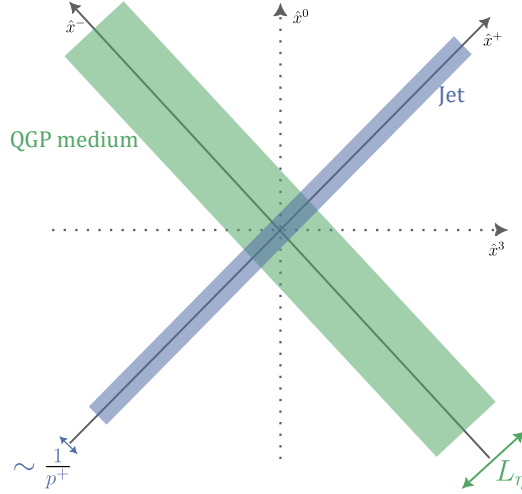


Fig. 1 Schematic representation of the jet evolution in a QGP medium.

2 Parton in-medium propagation

Jet quenching is due to the interaction of partons in a developing shower with the QGP they traverse. We consider the propagation of quarks and gluons, referring, whenever appropriate, to them jointly as partons or (hard) probes.

Hard partons propagating through QGP are, owing to their highly boosted kinematics, more conveniently described using light-cone coordinates¹.

The QGP is modelled as an external classical stochastic colour field as in [17], and further detailed in Appendix A. It is given by $\mathcal{A}^\mu = (\mathcal{A}^+, \mathcal{A}^\perp, \mathcal{A}^-)$, assumed to be boosted along the \hat{x}^- direction, and to have a finite length L_η in the \hat{x}^+ direction. A schematic representation of the parton propagation in the QGP under the above conditions is shown in Figure 1.

Since the parton is assumed to be propagating in the \hat{z} direction and that it is highly boosted ($p^z \gg \mathbf{p}$), the dominant component of the parton's light-cone momentum is p^+ . Furthermore, because the parton is highly localised in x^- , the smaller component of the momentum is p^- , i.e., $p^+ \gg \mathbf{p} > p^-$. As consequence, in this regime, the spacetime dependence of the field can be simplified to $\mathcal{A}^\mu(x^+, \mathbf{x}, x^-) \approx \mathcal{A}^\mu(x^+, \mathbf{x}, 0) \equiv \mathcal{A}^\mu(x^+, \mathbf{x})$. In the light-cone gauge ($\mathcal{A}^+ = 0$), the background field can be written as $\mathcal{A}^\mu = (\mathcal{A}^+, \mathcal{A}^\perp, \mathcal{A}^-) \equiv (\mathcal{A}^\perp, \mathcal{A}^-)$. Given the smallness of \mathcal{A}^\perp , the background field A^μ can be simplified to have \mathcal{A}^- as the only non-zero component, i.e., $A^\mu(x^+, \mathbf{x}) \equiv \mathcal{A}^-(x^+, \mathbf{x})$.

Under the sub-eikonal approximation², parton propagation in the medium resembles that of a 2D non-relativistic quantum system. The in-medium scalar propagator of a parton in the transverse plane, from $(0, \mathbf{y})$ to (x^0, \mathbf{x}) , is the Green's function $G(x^0, \mathbf{x}; 0, \mathbf{y})$ of the Schrödinger equation [5]

$$\left(i\partial_{x^0} + \frac{\partial_{\mathbf{x}}^2}{2p^+} + g\mathcal{A}^-(x^0, \mathbf{x}) \right) G(x^0, \mathbf{x}; 0, \mathbf{y}) = i\delta(x^0)\delta(\mathbf{x} - \mathbf{y}), \quad (1)$$

where g is a coupling constant. Here, $\mathcal{A}^-(x^0, \mathbf{x})$ is generically encapsulating both the quark and gluon cases. For the quark case it is defined as

$$\mathcal{A}^-(x^0, \mathbf{x}) \equiv \mathcal{A}_a^-(x^0, \mathbf{x}) \cdot \mathbf{t}^a, \quad (2)$$

where $\mathbf{t} \equiv \frac{\lambda}{2}$ with λ the SU(3) generators and a ranging from 1 to 8. Similarly, for the gluon case we have

$$\mathcal{A}^-(x^0, \mathbf{x}) \equiv -i\mathcal{A}_a^-(x^0, \mathbf{x}) \cdot \mathbf{T}^{aT}, \quad (3)$$

where \mathbf{T} are the generators in the adjoint representation, and \mathbf{T}^T are the transpose of \mathbf{T} .

According to Eq. 1, the Hamiltonian that describes the evolution of the parton in the medium is

$$\hat{H}_{q/g}(x^0) = \frac{\hat{\mathbf{p}}^2}{2p^+} + g\mathcal{A}^-(x^0, \mathbf{x}) = \hat{K} + \hat{V}(x^0). \quad (4)$$

The first term $\hat{K} = \frac{\hat{\mathbf{p}}^2}{2p^+}$ corresponds to the kinetic energy of the parton, with the light-cone energy p^+ playing the role of mass, and the second term $\hat{V}(x^0) = g\mathcal{A}^-(x^0, \mathbf{x})$ corresponds to the potential energy, which is time-dependent. The Hamiltonian $\hat{H}_{q/g}(x^0)$ rules the evolution of a single parton in the medium, with the subscript q

¹We write the four-momentum of a parton as $p = (p^+, \mathbf{p}, p^-)$, where $p^+ = \frac{p^0 + p^3}{2}$ corresponds to the light-front energy, \mathbf{p} is the transverse momentum and $p^- = p^0 - p^3$. Space-time coordinates are written as $x = (x^+, \mathbf{x}, x^-)$, where $x^+ = \frac{x^0 + x^3}{2}$ corresponds to the light-cone time, \mathbf{x} is the transverse position and $x^- = x^0 - x^3$. Parton propagation is assumed to be along the \hat{z} direction.

²The eikonal approximation is usually relaxed to allow small momentum transfers, with the light-cone energy still being conserved, which is known as the sub-eikonal approximation.

Gauge Group	Colour degrees of freedom		Casimir invariant	
	Quark	Gluon	C_F	C_A
SU(3)	3	8	$\frac{4}{3}$	3

Table 1 colour degrees of freedom of both quarks and gluons and Casimir invariants for the SU(3) gauge group. The Casimir invariants are defined as $C_F = \frac{N^2-1}{2N}$ and $C_A = N$ for the SU(N) group.

for a quark, the subscript g for a gluon, and the subscript q/g referring to both cases. The Hamiltonian can be re-written as a function of the light-cone time x^+

$$\hat{H}_{q/g}(x^+) = \frac{\hat{\mathbf{p}}^2}{2p^+} + g\mathcal{A}^-(x^+, \mathbf{x}) = \hat{K} + \hat{V}(x^+). \quad (5)$$

This Hamiltonian serves as the foundation for developing a quantum algorithm to simulate the parton's in-medium propagation.

3 Towards parton evolution in a quantum computer

To study the evolution of a system governed by the Hamiltonian in Eq. 5 in a quantum computer, the time evolution operator needs to be defined. In light-cone coordinates, x^+ represents the time dimension in which the medium extends over L_η . Thus, the time evolution operator for the entire medium extension can be written as

$$\hat{U}(L_\eta) \equiv \mathcal{T}_+ e^{-i \int_0^{L_\eta} dx^+ \hat{H}_{q/g}(x^+)}. \quad (6)$$

This operator acts on a two-dimensional Hilbert space, which is either spanned by the momentum eigenstates $|p\rangle$ or the position eigenstates $|x\rangle$. The time evolution operator evolves the system along the entire longitudinal extension of the medium, transforming the initial state $|\psi_0\rangle$ into a final state $|\psi_{L_\eta}\rangle = \hat{U}(L_\eta) |\psi_0\rangle$. The operator in Eq. 6 can be decomposed non-perturbatively into the sequential product of the same operator but for small time intervals of size Δ_{x^+} , i.e.,

$$\hat{U}(L_\eta; 0) = \prod_{j=0}^{N_t-1} \hat{U}(x_{j+1}^+; x_j^+), \quad (7)$$

with $x_j^+ = j\Delta_{x^+}$, $\Delta_{x^+} = \frac{L_\eta}{N_t}$, and N_t the number of time steps. In each time step, due to its small size, the time evolution operator can be approximated as the product of the evolution of the kinetic and potential terms. This approximation has corrections of the order of $\Delta_{x^+}^2$, such that, when $N_t \rightarrow \infty$, $\Delta_{x^+} \rightarrow 0$, it becomes exact with the time evolution operator for the whole medium extension being retrieved. This approximation also facilitates mapping the time evolution operator into a quantum circuit.

To implement the evolution on a quantum computer and retrieve information from the final state $|\psi_{L_\eta}\rangle$, the three major steps of the quantum simulation algorithm [19] need to be well-defined as described in the following subsections. The algorithm developed here assumes that the medium probe, the hard parton, is ruled by the SU(3) gauge group, being either a quark or a gluon. The colour degrees of freedom of both quarks and gluons and their Casimir invariants are summarised in Table 1. Furthermore, since the kinetic term of the Hamiltonian is diagonal in the momentum basis, and the potential term is diagonal in the position basis, the algorithm is developed in a mixed representation where the momentum and position bases are both used.

3.1 Embedding and initialization

The system's data is embedded into quantum states using the basis embedding technique, i.e., the classical bits are directly mapped into quantum bits. For instance, an n -qubit quantum state $|i\rangle = |i_0 i_1 \dots i_n\rangle$ represents the classical value $i = i_0 i_1 \dots i_n$, where i_0, i_1, \dots, i_n are the classical bits. The two-dimensional Hilbert space essentially corresponds to the two dimensions of the transverse lattice, i.e., \hat{x} and \hat{y} directions. Since the algorithm is developed in a mixed position-momentum basis, the change of basis, between the momentum and position bases, is performed using the Quantum Fourier Transform (QFT) [19], which is detailed in subsection 3.2.

The transverse lattice is a two-dimensional lattice, with $2N_\perp$ sites per direction with each direction extending from $-L_\perp$ to L_\perp . The spacing of the lattice is then $\Delta_\perp = \frac{2L_\perp}{2N_\perp} = \frac{L_\perp}{N_\perp}$, in the position basis. Consequently, the lattice spacing in the momentum basis is $\Delta_{\perp p} = \frac{2\pi}{2L_\perp} = \frac{\pi}{L_\perp}$, which corresponds to the reciprocal lattice spacing. The discrete lattice states $|n_x, n_y\rangle$ and $|k_x, k_y\rangle$ are related to the continuum ones $|x, y\rangle$ and $|p_x, p_y\rangle$ by

$$|x, y\rangle \equiv \Delta_\perp |n_x, n_y\rangle, \quad n_x, n_y \in \{-N_\perp, -N_\perp + 1, \dots, 0, \dots, N_\perp - 1\}, \quad (8)$$

and

$$|p_x, p_y\rangle \equiv \Delta_{\perp p} |k_x, k_y\rangle \quad k_x, k_y \in \{-N_\perp, -N_\perp + 1, \dots, 0, \dots, N_\perp - 1\}. \quad (9)$$

A periodic boundary condition is imposed on the lattice, with points separated by an integer multiple of the period $2L_\perp$ being identified:

$$\hat{O} |n_x, n_y\rangle = \hat{O} |n_x + i2N_\perp, n_y + j2N_\perp\rangle, \quad (10)$$

and

$$\hat{O} |k_x, k_y\rangle = \hat{O} |k_x + i2N_\perp, k_y + j2N_\perp\rangle, \quad (11)$$

with $i, j \in \mathbb{Z}$ and \hat{O} a generic operator. This periodic condition identifies the states $|n_i, n_j\rangle$ with $n_i, n_j \in \{-N_\perp, -N_\perp + 1, \dots, -1\}$ with the ones with $n_i, n_j \in \{N_\perp, N_\perp + 1, \dots, 2N_\perp - 1\}$, and the same for the momentum basis, allowing us to work in the interval $[0, 2N_\perp - 1]$ for both the position and momentum bases. Working in this interval not only facilitates the basis change through the QFT/QFT † , but also simplifies the basis embedding due to the non-negativity of the indices. Using basis embedding, the system's state can simply be written

$$|n_x, n_y\rangle \equiv |n_{x_0} n_{x_1} \dots n_{x_{\log_2(2N_\perp)}}, n_{y_0} n_{y_1} \dots n_{y_{\log_2(2N_\perp)}}\rangle, \quad (12)$$

and

$$|k_x, k_y\rangle = |k_{x_0} k_{x_1} \dots k_{x_{\log_2(2N_\perp)}}, k_{y_0} k_{y_1} \dots k_{y_{\log_2(2N_\perp)}}\rangle, \quad (13)$$

where $n_{x_i}, n_{y_i}, k_{x_i}, k_{y_i} \in \{0, 1\}$. Consequently, to encode the position/momentum information in the quantum state, we need $n_q \equiv \log_2(2N_\perp)$ qubits per direction. The qubits representing the position/momentum form two registers, one for each direction.

Besides the transverse lattice, the system's state also encodes information about the colour of the parton. The colour of the parton is also embedded using basis embedding, and, for the SU(3) gauge group, when the parton is a quark, there are three possible colours, and so two qubits are needed to encode the colour information, and when the parton is a gluon, three qubits are needed to encode the colour information. The qubits representing the colour form also a register, the colour register. The system's state is then a tensor product of the transverse lattice state ($|n_x, n_y\rangle$ or $|k_x, k_y\rangle$) and the colour state ($|c\rangle$), i.e., $|n_x, n_y, c\rangle$ or $|k_x, k_y, c\rangle$.

Regarding the initialization, the transverse lattice is initialised in the zero momentum state, i.e., $|0, 0\rangle$, unless initial momentum effects are of interest. The colour of the parton is initialised in a uniform superposition.

3.2 Encoding and evolution

After establishing how the system's data is embedded in quantum states, the time evolution operator in Eq. 6 needs to be discretised and translated into a quantum circuit according to the chosen qubit embedding. Attending to Eq. 7, one only needs to define the time evolution operator for a small time interval Δx^+ , i.e., $\hat{U}(x_{j+1}^+; x_j^+)$. Then, the whole time evolution operator is simply the product of these operators. In the context of quantum circuits, this means that one needs to know how to implement the time evolution operator for a small time interval, and then the whole time evolution is simply the sequential application of these operators.

The Hamiltonian defined in Eq. 5 has a time dependence only in the potential term, and so the kinetic operator remains the same in the whole evolution. The time dependence of the potential term arises from the background field. Consequently, to include this time dependence, the background field is sliced into N_η intervals of size $\Delta_\eta = \frac{L_\eta}{N_\eta}$. In each slice, the background field is assumed to be constant and is generated in a classical computer. Since the medium is assumed to be constant in each slice Δ_η , the time steps Δ_{x^+} should not be larger than Δ_η , i.e., $\Delta_{x^+} \leq \Delta_\eta$. For a sufficiently small time step Δ_{x^+} , the time evolution operator for each interval Δ_{x^+} can be approximated as the product of the evolution of the kinetic and potential terms, and thus written as

$$\hat{U}(x_{j+1}^+; x_j^+) = \hat{U}(x_j^+ + \Delta_{x^+}; x_j^+) = e^{-i\hat{H}_{q/g}(x_j^+)\Delta_{x^+}} \approx e^{-i\frac{\mathbf{p}^2}{2p^+}\Delta_{x^+}} e^{-igA^-(x_j^+, \mathbf{x})\Delta_{x^+}}. \quad (14)$$

When the parton is a quark, this operator is explicitly written as

$$\hat{U}_q(x_j^+ + \Delta_{x^+}; x_j^+) \approx e^{-i\frac{\mathbf{p}^2}{2p^+}\Delta_{x^+}} e^{-igA_a^-(x_j^+, \mathbf{x})\mathbf{t}^a\Delta_{x^+}}, \quad (15)$$

and for a gluon

$$\hat{U}_g(x_j^+ + \Delta_{x^+}; x_j^+) \equiv e^{-i\frac{\mathbf{p}^2}{2p^+}\Delta_{x^+}} e^{-igA_a^-(x_j^+, \mathbf{x})\mathbf{T}^{a'}\Delta_{x^+}}, \quad (16)$$

where $\mathbf{T}^{a'} = -i\mathbf{T}^{aT}$.

Since the kinetic term is diagonal in the momentum basis and the potential term is diagonal in the position basis, the implementation of the time evolution operator in each step benefits from a mixed space representation: the kinetic operator is applied in the momentum basis; and, the potential operator is applied in the position basis. Although the operator could be applied in other bases, namely only on the momentum or only on the position basis, the mixed space representation is chosen since it promotes a more straightforward quantum implementation. Within the mixed-state representation, in each time step, the evolution operator corresponds then to the implementation of the kinetic term in the momentum basis, the QFT † to change to the position basis, followed by the application

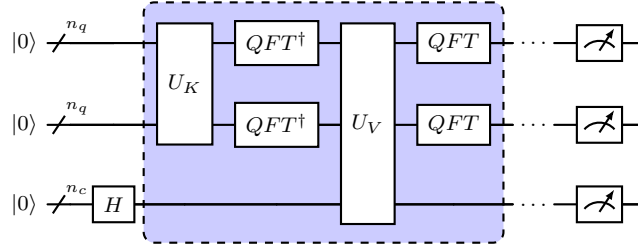


Fig. 2 Quantum circuit for the quantum simulation of a parton propagating in a QGP medium, where n_c is the number of colour qubits and n_q is the number of position/momentum qubits per direction. The first step is the initialization, the second step is the application of the time evolution operator, and the third step is the measurement of the final system state. The U_K and U_V are the kinetic and potential evolution operators, respectively, and the QFT and QFT^\dagger are the gate representation of the QFT and its inverse, respectively. Inside the dashed box, one iteration of the time evolution operator is shown.

of the potential term in the position basis, and, finally, the QFT to change back to the momentum basis. This framework is summarised as a quantum circuit in Figure 2, where the dashed box represents one iteration of the time evolution operator, and the initialization and measurement are also included.

The implementation of the QFT and QFT^\dagger follows the framework described in [19]. The implementation of the kinetic and potential terms is described separately below.

3.2.1 Kinetic term

For each time slice, the time evolution of the kinetic operator is given by

$$U_K = e^{-i \frac{\hat{\mathbf{p}}^2}{2p^+} \Delta_{x^+}} = e^{-i \frac{\hat{p}_x^2 + \hat{p}_y^2}{2p^+} \Delta_{x^+}}. \quad (17)$$

The first step is to implement the square of the momentum operator, i.e., $\hat{\mathbf{p}}^2 = \hat{p}_x^2 + \hat{p}_y^2$, in the momentum basis where the momentum operator is diagonal, and then exponentiate it. The effect of applying \hat{p}^2 to a momentum state $|p_x, p_y\rangle$ is

$$\hat{\mathbf{p}}^2 |p_x, p_y\rangle = (p_x^2 + p_y^2) |p_x, p_y\rangle. \quad (18)$$

Knowing that the lattice momentum states $|k_x, k_y\rangle$ are related to the momentum states $|p_x, p_y\rangle$ by $|p_x, p_y\rangle = \Delta_{\perp p}^2 |k_x, k_y\rangle$, the effect of applying \hat{p}^2 to a momentum state $|k_x, k_y\rangle$ is

$$\hat{\mathbf{p}}^2 |k_x, k_y\rangle = \Delta_{\perp p}^2 (k_x^2 + k_y^2) |k_x, k_y\rangle. \quad (19)$$

Therefore, the elements of the \hat{p}^2 operator in the momentum basis are determined by

$$\langle k'_x, k'_y | \hat{\mathbf{p}}^2 |k_x, k_y\rangle = \Delta_{\perp p}^2 (k_x^2 + k_y^2) \delta_{k'_x, k_x} \delta_{k'_y, k_y}. \quad (20)$$

Now, one can directly exponentiate the \hat{p}^2 operator, i.e., $e^{-i \frac{\hat{\mathbf{p}}^2}{2p^+} \Delta_{x^+}}$ with p^+ and Δ_{x^+} as fixed parameters, and apply the resulting unitary operator to the momentum states. The creation of a unitary gate from a unitary operator/matrix is done using the `UnitaryGate` class from the Qiskit library [20].

3.2.2 Potential term

As for the kinetic term, in each time slice, one needs to implement the time evolution operator as a quantum circuit. This operator is given by

$$\hat{U}_{V_q} = e^{-ig \mathcal{A}_a^-(x_j^+, \mathbf{x}) \mathbf{t}^a \Delta_{x^+}}, \quad (21)$$

for a quark, and

$$\hat{U}_{V_g} = e^{-ig \mathcal{A}_a^-(x_j^+, \mathbf{x}) \mathbf{T}^{a'} \Delta_{x^+}}, \quad (22)$$

for a gluon.

The potential term is diagonal in the position basis, and so the implementation of the potential term is carried out on this basis. The first step in the implementation of the potential term is to generate the background field on a classical computer, as described in Appendix A. Then, the values of the background field need to be contracted with the colour generators for the quark case, or with the structure constants for the gluon case. This contraction can be performed in two different ways, which are both explored and compared. Both methodologies require the representation of the background field as a diagonal matrix in the position basis, denoted as $\hat{\mathcal{A}}^-(x_j^+, \mathbf{x})$. When the matrix form of the colour generators has a different shape than $2^{n_c} \times 2^{n_c}$, where n_c is the number of colour qubits, the matrices should be padded with zeros to achieve the correct shape. The same padding rule applies to the $\mathbf{T}^{a'}$ matrices.

The two implementations of colour evolution are as follows:

- The first one consists of contracting the background field with the colour generators or structure constants through a tensorial product, i.e., the matrix form of the background field is tensored with the colour generators or the transpose of the matrix form of the structure constants multiplied by $-i$. In this context, being $\hat{\mathcal{A}}_a^-$ the a^{th} component of the background field operator in the matrix form, the contraction with the colour generators is given by $\sum_{a=1}^{N^2-1} \hat{\mathcal{A}}_a^- \otimes \mathbf{t}^a$, and with the matrices $\mathbf{T}^{a'}$ is given by $\sum_{a=1}^{N^2-1} \hat{\mathcal{A}}_a^- \otimes \mathbf{T}^{a'}$. After computing the sum of tensorial products, the resulting operator can be directly done using the `UnitaryGate` class from the Qiskit library [20], or through the decomposition of the operator into a sum of Pauli strings and then exponentiating the Pauli strings. The resulting operator should act in all the qubits, i.e., the position and colour qubits.
- The second method starts by inferring that the operator \hat{U}_V can be written as the product of the evolution of each colour component, i.e., $\hat{U}_V = \hat{U}_{V_1} \hat{U}_{V_2} \dots \hat{U}_{V_{N^2-1}}$, with $\hat{U}_{V_{a_q}} = e^{-ig\hat{\mathcal{A}}_a^- \mathbf{t}^a \Delta_{x^+}}$, for the quark, and $\hat{U}_{V_{a_g}} = e^{-ig\hat{\mathcal{A}}_a^- \mathbf{T}^{a'} \Delta_{x^+}}$, for the gluon. Then, the next step consists of verifying that all the matrices \mathbf{t}^a and $\mathbf{T}^{a'}$ have eigenvalues 1 and -1 . Thus, for each colour component, when the colour state is in the eigenstates with eigenvalue 1, the operator $e^{-ig\hat{\mathcal{A}}_a^- \Delta_{x^+}}$ should be applied on the position qubits, and when the eigenstate has eigenvalue -1 , the operator $e^{ig\hat{\mathcal{A}}_a^- \Delta_{x^+}}$ should be applied on the position qubits. Finally, in this way, the operators \hat{U}_{V_a} are applied through controlled operations, with the colour qubits being the control qubits, and the position qubits being the target qubits. As an example, the implementation of the first colour component of a SU(3) quark can be found in [16].

3.3 Measurement and post-processing

The last component of the quantum simulation is the measurement. Although one could implement a sophisticated measurement procedure to extract any desired property from the system's final state – such as the one proposed in [16] to directly extract the jet quenching parameter \hat{q} –, here we chose to retrieve the full probability distribution and then post-process that data. The jet quenching parameter \hat{q} , which is a very relevant quantity in the context of jet quenching, is physically defined as the rate of the transverse momentum broadening [21].

By measuring all the qubits, one directly retrieves from the quantum computer the probability distribution of the system's final state, i.e., the probability of finding the system in each of the possible states. The lattice registers are measured on the momentum basis. Recalling the chosen embedding scheme (subsection 3.1), the measured states are in the form $|k_x, k_y, c\rangle = |k_{x_0} \dots k_{x_{n_q-1}}, k_{y_0} \dots k_{y_{n_q-1}}, c_0 \dots c_{n_c-1}\rangle$, with n_c being the number of colour qubits. The measured states then need to be post-processed to extract the probability distribution of the squared transverse momentum. This post-processing is done in four major steps:

1. The measured states are converted from the binary representation to the decimal representation;
2. The lattice is recentered, i.e., the values larger than N_\perp are subtracted by $2N_\perp$, and so the values are in the range $[-N_\perp, N_\perp)$ instead of $[0, 2N_\perp)$;
3. The lattice values are converted to the physical values, with the lattice values being multiplied by $\Delta_{\perp p}$, i.e., $|k_x, k_y\rangle \rightarrow |k_x \Delta_{\perp p}, k_y \Delta_{\perp p}\rangle = |p_x, p_y\rangle$;
4. The squared transverse momentum is computed, i.e., $p^2 = p_x^2 + p_y^2$.

We note that when the colour register is initialised in a uniform superposition containing states without physical meaning, i.e. for a SU(3) quark where two qubits are used to encode the three possible colours, the spurious states should be removed from the momentum distribution and, consequently, the distribution should be renormalised.

To better compare the simulation data with the analytical results, it is convenient to consider the transverse momentum transferred by the medium to the parton, commonly referred to as the saturation scale Q_s^2 , which, in the fundamental representation and neglecting logarithmic corrections, is given by

$$Q_s^2 = C_F \frac{(g^2 \mu^2)^2 L_\eta}{2\pi}, \quad (23)$$

where $C_F = \frac{N_c^2-1}{2N_c}$ is the fundamental Casimir of the SU(N_c) group.

Besides the direct plots and analysis of the probability distribution, determining the jet quenching parameter \hat{q} and comparing it with the analytical results is also of interest. The jet quenching parameter \hat{q} can be extracted from the probability distributions for different background fields through

$$\hat{q} \equiv \frac{\langle\langle \hat{\mathbf{p}}^2(L_\eta) \rangle\rangle - \langle\langle \hat{\mathbf{p}}^2(0) \rangle\rangle}{L_\eta}, \quad (24)$$

where $\langle\langle \dots \rangle\rangle$ denotes the average over different background field configurations, and $\langle \hat{\mathbf{p}}^2(x) \rangle$ denotes the probability weighted average of the squared transverse momentum at the light-front time x . When one does not want to study the effect of initial transverse momentum, the initial transverse momentum is set to zero, with the jet quenching parameter being simply given by

$$\hat{q} \equiv \frac{\langle\langle \hat{\mathbf{p}}^2(L_\eta) \rangle\rangle}{L_\eta}. \quad (25)$$

The \hat{q} extracted from the simulation is compared with its analytical counterpart, i.e.,

$$\hat{q}_{q/g} = \frac{g^4 \mu^2 C_{F/A}}{4\pi} \left(\log \left(\frac{1 + \frac{\Delta_\perp^2 m_g^2}{\pi^2}}{\frac{1}{N_\perp^2} + \frac{\Delta_\perp^2 m_g^2}{\pi^2}} \right) - \frac{\Delta_\perp^2 m_g^2}{\pi^2} \left(\frac{1}{\frac{1}{N_\perp^2} + \frac{\Delta_\perp^2 m_g^2}{\pi^2}} - \frac{1}{1 + \frac{\Delta_\perp^2 m_g^2}{\pi^2}} \right) \right), \quad (26)$$

A detailed derivation of Eq. 26 can be found in Appendix B.

3.4 Discrete lattice effects

The use of a discrete lattice to simulate the parton propagation in a gauge field can lead to undesired lattice effects in the results. These lattice effects can be avoided by the right choice of some of the simulation parameters. Such as in [17], one is interested in avoiding two main effects: (1) ensuring that the lattice spacing captures all the relevant physics – *spacing effects* – and (2) ensuring that the assumption that the lattice is finite does not affect the results – *finite size effects*.

The discrete nature of the lattice introduces two cutoffs, an IR cutoff $\lambda_{IR} = \frac{\pi}{L_\perp}$ and an UV cutoff $\lambda_{UV} = \frac{\pi}{\Delta_\perp} = \lambda_{IR} N_\perp$.

To ensure the absence of *spacing effects*, the lattice spacing Δ_\perp should be chosen in such a way that the momentum transfer Q_s is much smaller than the UV cutoff λ_{UV} , i.e.,

$$Q_s \ll \lambda_{UV} \Rightarrow Q_s \ll \frac{\pi}{\Delta_\perp} \Rightarrow \Delta_\perp \ll \frac{\pi}{Q_s}, \quad (27)$$

and that the physical IR regulator m_g is much larger than the IR cutoff λ_{IR} , i.e.,

$$m_g \gg \lambda_{IR} \Rightarrow m_g \gg \frac{\pi}{L_\perp} \Rightarrow L_\perp \gg \frac{\pi}{m_g} \Rightarrow N_\perp \Delta_\perp \gg \frac{\pi}{m_g} \Rightarrow \Delta_\perp \gg \frac{\pi}{N_\perp m_g}. \quad (28)$$

Jointly, these two conditions lead to

$$\frac{\pi}{N_\perp m_g} \ll \Delta_\perp \ll \frac{\pi}{Q_s}. \quad (29)$$

Due to the lattice periodicity, when there are *finite size effects*, the lattice edges affect the final momentum distribution by making it asymptotically uniform. Mathematically, a uniform momentum distribution can be described as

$$\begin{aligned} \langle \mathbf{p}^2 \rangle &\xrightarrow{L_\eta \gg 0} \frac{1}{(2N_\perp)^2} \sum_{k_x=-N_\perp}^{N_\perp-1} \sum_{k_y=-N_\perp}^{N_\perp} (k_x^2 + k_y^2) \Delta_{\perp p}^2 \\ &= \frac{1}{(2N_\perp)^2} \left(\frac{4}{3} N_\perp^2 (2N_\perp^2 + 1) \right) \Delta_{\perp p}^2 \\ &= \frac{2}{3} N_\perp^2 \Delta_{\perp p}^2 + \frac{1}{3} \Delta_{\perp p}^2 \approx \frac{2}{3} N_\perp^2 \Delta_{\perp p}^2 = \frac{2}{3} N_\perp^2 \left(\frac{\pi}{L_\perp} \right)^2 \\ &= \frac{2}{3} N_\perp^2 \left(\frac{\pi}{L_\perp} \right)^2 = \frac{2}{3} \frac{\pi^2}{\Delta_\perp^2} \equiv \langle \mathbf{p}^2 \rangle_{\text{uniform}}. \end{aligned} \quad (30)$$

Now, defining $L_{sat} \equiv \frac{\langle \mathbf{p}^2 \rangle_{\text{uniform}}}{\hat{q}}$, to avoid the uniform momentum distribution, one should ensure a set of parameters where $L_{sat} \gg L_\eta$, i.e., the total time of the evolution should be smaller than the time needed for the lattice edges to affect the final momentum distribution. For the quark case, recalling the expressions for Q_s^2 , Eq. 23, and \hat{q} , Eq. 26, this condition is rewritten as

$$\begin{aligned} L_{sat} \gg L_\eta &\Rightarrow \frac{2}{3} \frac{\pi^2}{\Delta_\perp^2 \hat{q}} \gg L_\eta \\ &\Rightarrow \frac{2}{\sqrt{3}} \frac{\pi}{Q_s \left(\log \left(\frac{1 + \frac{\Delta_\perp^2 m_g^2}{\pi^2}}{\frac{1}{N_\perp^2} + \frac{\Delta_\perp^2 m_g^2}{\pi^2}} \right) - \frac{\Delta_\perp^2 m_g^2}{\pi^2} \left(\frac{1}{\frac{1}{N_\perp^2} + \frac{\Delta_\perp^2 m_g^2}{\pi^2}} - \frac{1}{1 + \frac{\Delta_\perp^2 m_g^2}{\pi^2}} \right) \right)^{\frac{1}{2}}} - \Delta_\perp \gg 0. \end{aligned} \quad (31)$$

Consequently, to avoid the *finite size effects* for a quark, one should ensure that this expression is positive.

For a gluon, the saturation scale is given by $\tilde{Q}^2 \equiv C_A \frac{(g^2 \mu)^2 L_\eta}{2\pi}$ and the gluon version of Eq. 31 is obtained by simply replacing $Q_s \rightarrow \tilde{Q}$.

Spacing effects are avoided for choices of Q_s^2, N_\perp, L_\perp , and m_g , for which Eq. 29 is satisfied.

Figure 3 shows the conditions regarding spacing effects, which are the same for quarks and gluons, for different choices of Q_s^2, N_\perp, L_\perp , and m_g . The conditions for finite size effects are shown, separately for quarks and gluons, in Figure 4 and Figure 5.

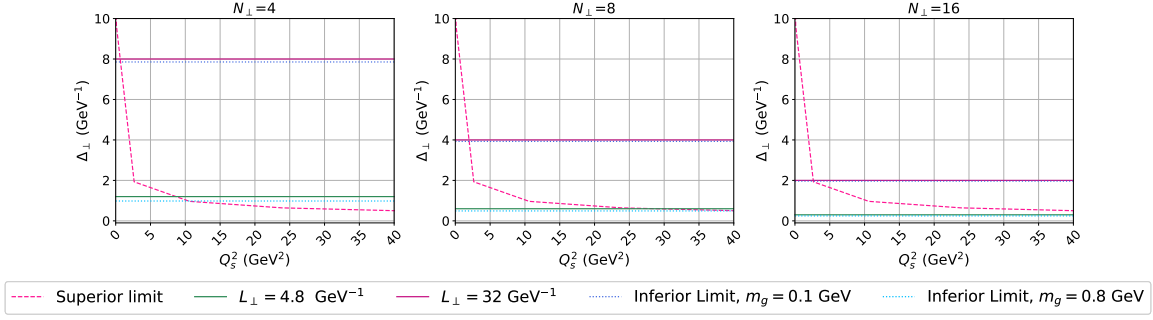


Fig. 3 Spacing effects for the SU(3) gauge group for $N_{\perp} \in [4, 8, 16]$, $L_{\perp} \in [4.8, 32]$ GeV $^{-1}$ and $m_g \in [0.1, 0.8]$ GeV for several values of $g^2\mu$. The upper limit corresponds to the condition $\Delta_{\perp} \ll \frac{\pi}{Q_s}$, and the lower limits corresponds to the condition $\Delta_{\perp} \gg \frac{\pi}{N_{\perp}m_g}$, one for each m_g value. The filled green and pink lines correspond to the two possible values of Δ_{\perp} for each value of N_{\perp} .

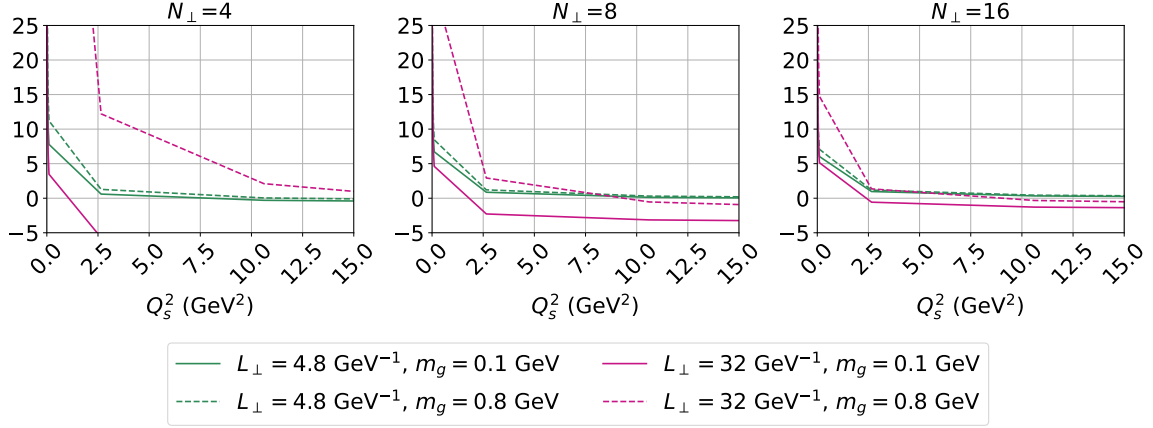


Fig. 4 Finite size effects for a SU(3) quark for $N_{\perp} \in [4, 8, 16]$, $L_{\perp} \in [4.8, 32]$ GeV $^{-1}$ and $m_g \in [0.1, 0.8]$ GeV for several values of $g^2\mu$. Each curve corresponds to the condition in Eq. 31 for the two possible values of Δ_{\perp} for each value of N_{\perp} , which are related to the L_{\perp} values.

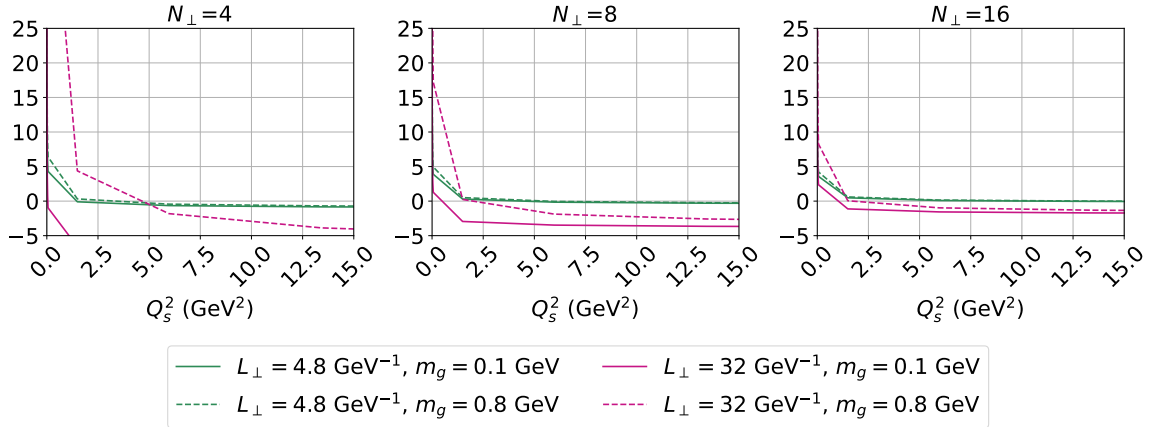


Fig. 5 Finite size effects for a SU(3) gluon for $N_{\perp} \in [4, 8, 16]$, $L_{\perp} \in [4.8, 32]$ GeV $^{-1}$ and $m_g \in [0.1, 0.8]$ GeV for several values of $g^2\mu$.

The most salient feature in Figure 3 is that for $m_g = 0.1$ GeV, using 4.8 GeV $^{-1}$ for L_{\perp} , leads to spacing effects for all values of $g^2\mu$ and N_{\perp} . This is the reason why when $L_{\perp} = 4.8$ GeV $^{-1}$, $m_g = 0.8$ GeV is chosen, and when $L_{\perp} = 32$ GeV $^{-1}$, $m_g = 0.1$ GeV is chosen. Concerning the upper limit, choosing $L_{\perp} = 4.8$ GeV $^{-1}$ and $m_g = 0.8$ GeV always allows a larger range of saturation scales that are not affected by spacing effects than choosing $L_{\perp} = 32$ GeV $^{-1}$, $m_g = 0.1$. Consequently, the former set of parameters will be used.

For the quark case, the larger the values of N_{\perp} , the smaller the values of Q_s^2 that lead to the finite effects, and the larger the values of N_{\perp} the larger the values of Q_s^2 that lead to the absence of the finite size effects. For $L_{\perp} = 32$ GeV $^{-1}$, the values become “more negative” than for $L_{\perp} = 4.8$ GeV $^{-1}$, which converge to a small value around 0 as Q_s^2 increases. Furthermore, for $m_g = 0.1$ GeV the lines tend to become negative for smaller values of Q_s^2 than for $m_g = 0.8$ GeV, which is more evident for smaller values of N_{\perp} .

When looking at the results in Figure 5, one can see that the morphology of the curves is quite similar to the ones for the quark case, in Figure 4, with the main and most significant different being the fact that the curves

Parameter (Units)	Value(s)
N_{\perp}	4, 8, 16
L_{\perp} (GeV ⁻¹)	4.8
N_{η}	4, 8, 16, 32, 64
L_{η} (GeV ⁻¹)	50
$g^2\mu$ (GeV ^{3/2})	0.004, 0.006, 0.008, 0.01, 0.03, 0.05, 0.06, 0.08, 0.1, 0.5, 1, 1.5, 2
p^+ (GeV)	$+\infty$, 200, 100, 50, 5, 1
N_{reps}	1, 2, 4
m_g (GeV)	0.8
g	1

Table 2 List of the parameters explored in the parton’s quantum simulations.

become negative for smaller values of Q_s^2 than for the quark case. Consequently, one can expect that the results found for the gluon case are more affected by the finite size effects than the ones for the quark case, especially for the higher values of Q_s^2 .

4 Results and analysis

As seen in section 3, SU(3) parton propagation can be performed using different implementations of the potential term: via tensorial product (*tensorial* method); and via multiple controlled operations (*controlled*).

For both a SU(3) quark and a SU(3) gluon, one wants to essentially understand the impact of five parameters: N_{reps} , Δ_{\perp} , N_{η} , $g^2\mu$ and p^+ . The first one, N_{reps} , is the number of subdivisions of each medium slice N_{η} , i.e., for each longitudinal medium slice in how many time steps the quark is evolved, which is closely related to the time step Δ_{x^+} . The other four parameters were already well discussed. The full set of parameters explored in the quantum simulations is presented in Table 2. The only parameters that were a priori chosen to avoid undesired lattice effects are L_{\perp} and m_g .

For each study and for each set of parameters, the \hat{q} is calculated from the retrieved momentum distributions, following Eq. 25, and compared to the analytical expectation obtained from Eq. 26. This comparison is always made for different values of p^+ and Q_s^2 , which is computed with Eq. 23 from the $g^2\mu$ value. Furthermore, for each set of parameters, three different executions of the quantum circuit are performed, corresponding to different background field configurations. Each point in the plot is the mean of the three individual executions and the error bars are their standard deviation.

The decomposition of the quantum operators in quantum gates is always performed using the `UnitaryGate` class from Qiskit’s framework [20]. This choice is made since the majority of the studies performed here are executed in simulation environments and the decomposition of the operators into a sum of Pauli matrices brings additional time to the simulation. Furthermore, due to the large size and depth of the quantum circuits, obtained using both methods, the results using a real quantum device are expected to be severely affected by the noise and the decoherence of the quantum device, and so the use of a more time-consuming method is not justified.

The quantum simulations are implemented using Qiskit’s framework [20]. The quantum circuits are almost always executed using the `qasm_simulator` backend, which is a quantum computer simulator, with the number of shots in each execution being 10000. Due to the actual state of development of quantum devices and their limited access, only a few preliminary quantum simulations were executed in a real quantum device. The simulations were performed on `ibm_brisbane` device, an `Eagle r3` processor, and it was found that the noise completely surpasses the signal, leading to meaningless results. Although this result is not desired, it is expected since error mitigation techniques weren’t used, and the circuits are large and complex.

4.1 Quark

Although not very informative, the first step to analyse the simulation results is to look at the squared momentum distribution retrieved from the quantum computer. The squared momentum distribution for a SU(3) quark with $N_{\perp} = 8$, $L_{\perp} = 4.8$ GeV⁻¹, $m_g = 0.8$ GeV, $N_{\eta} = 4$, $p^+ = +\infty$ GeV, $g^2\mu = 0.5$ GeV^{3/2} and $N_{reps} = 1$ is in Figure 6. This figure shows the usual tail-shaped momentum distribution, but, apart from that, it isn’t easy to compare the results with the analytical expectation and analyse them.

Concerning the impact of the N_{reps} parameter, the same conclusions were always retrieved for the different values of N_{\perp} analysed. Therefore, we show in Figure 7 its impact on the jet quenching parameter for several saturation scales, several values of p^+ , $N_{reps} \in \{1, 2, 4\}$ and the two implementation methods, with $N_{\perp} = 8$, $L_{\perp} = 4.8$ GeV⁻¹, $m_g = 0.8$, $N_{\eta} = 16$. The analytical expectation Eq. 26 is also shown for comparison. The increase of the value of N_{reps} leads to worse results, i.e., more distant from the analytical expectation, mainly for

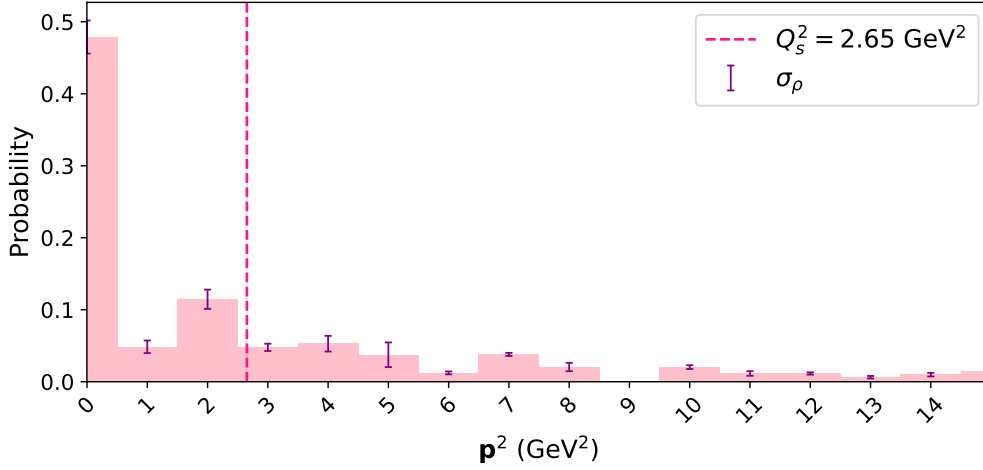


Fig. 6 Squared momentum distribution for a SU(3) quark with $N_{\perp} = 8$, $L_{\perp} = 4.8 \text{ GeV}^{-1}$, $m_g = 0.8 \text{ GeV}$, $N_{\eta} = 4$, $p^+ = +\infty \text{ GeV}$, $g^2\mu = 0.5 \text{ GeV}^{\frac{3}{2}}$ and $N_{reps} = 1$. For this plot, three individual executions of the quantum circuit are presented, with the height of the bins being the mean of the three individual executions and the error bars being the respective standard deviation. Each execution corresponds to a different background field configuration. The vertical dashed line represents the saturation scale of that simulation.

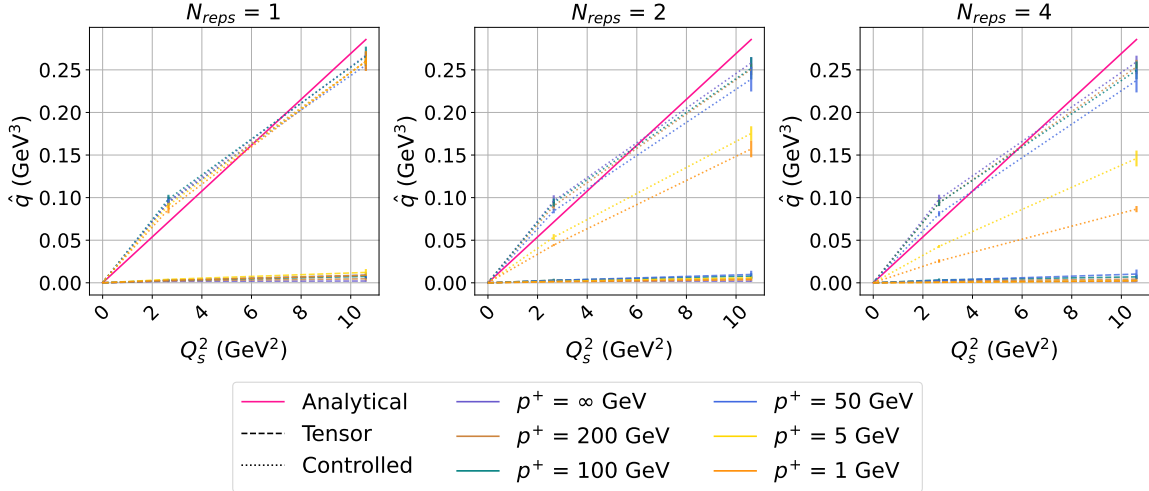


Fig. 7 Jet quenching parameter \hat{q} as a function of the saturation scale Q_s^2 for a SU(3) quark with $N_{\perp} = 8$, $L_{\perp} = 4.8 \text{ GeV}^{-1}$, $m_g = 0.8$, $N_{\eta} = 16$ for several values of p^+ . For each set of parameters, three different executions of the quantum circuit are performed, for different background field configurations, consequently, each point in the plot is the mean of the three individual executions and the error bars are the respective standard deviation. The solid lines represent the analytical expectations.

smaller values of p^+ . Consequently, the value of N_{reps} is fixed to 1 in the other studies. Importantly, only the controlled method is in agreement with the analytical expectation. The discrepancy between the methods should be explained by numerical and simulation errors: the tensorial method implies the tensor product of the colour generators matrices by diagonal matrices representing the colour field values, which are small numbers, leading to a large sparse matrix where the non-zero elements are small numbers; then, this matrix is exponentiated, which adds more numerical errors; and, finally, the matrix needs to be converted into quantum gates, which is a process that relies on approximations, introducing more errors. In comparison, the controlled method only requires exponentiating the matrices representing the colour generators component by component and then converting them into quantum gates, which is a much simpler procedure.

Even though the impact of the N_{η} parameter was studied for different values of N_{\perp} , the considered values of N_{η} are different for each given N_{\perp} . The larger the N_{\perp} and N_{η} , the slower and more resource consuming are the simulations. Although increasing the N_{η} value leads to convergent results respecting the different p^+ values, the convergence for small values of N_{η} makes the improvement difficult to see in Figure 8, Figure 9 and Figure 10.

When comparing different N_{\perp} values, one can easily infer that the larger the N_{\perp} value, the larger the range of saturation scales that lead to results in a good agreement with the classical expectation. This result is explained by the spacing effects present in the simulations (see Figure 3).

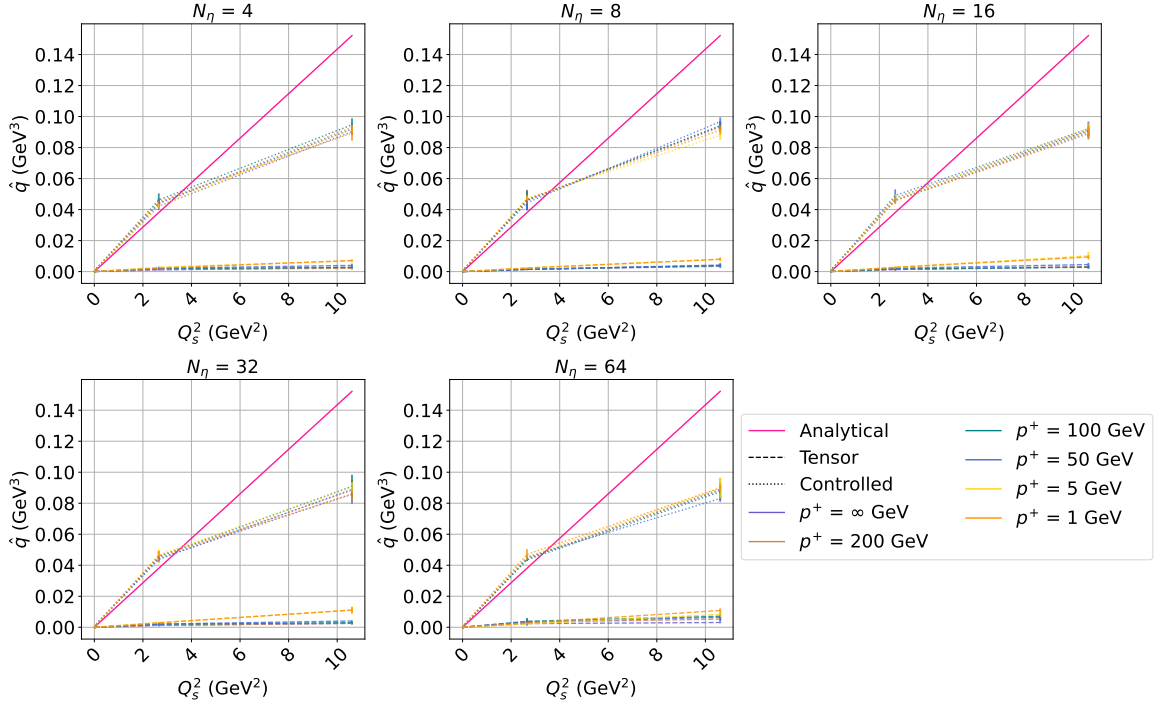


Fig. 8 Jet quenching parameter \hat{q} as a function of the saturation scale Q_s^2 for a SU(3) quark with $N_\perp = 4$, $L_\perp = 4.8 \text{ GeV}^{-1}$, $N_{reps} = 1$, $m_g = 0.8 \text{ GeV}$ for several values of p^+ and N_η . For each set of parameters, three different executions of the quantum circuit are performed, for different background field configurations, consequently, each point in the plot is the mean of the three individual executions and the error bars are the respective standard deviation. The solid lines represent the analytical expectations.

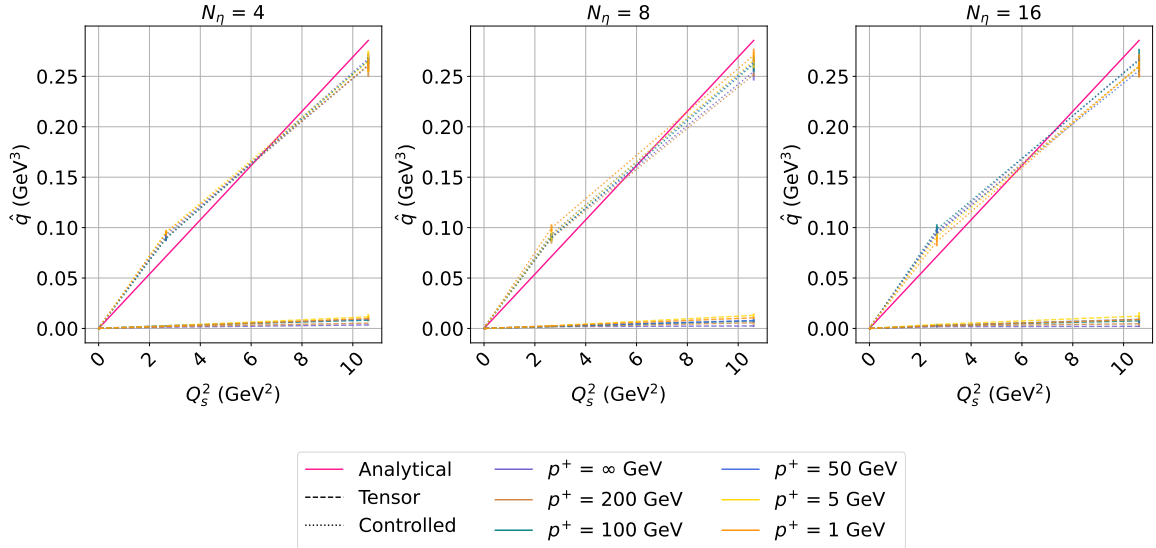


Fig. 9 Jet quenching parameter \hat{q} as a function of the saturation scale Q_s^2 for a SU(3) quark with $N_\perp = 8$, $L_\perp = 4.8 \text{ GeV}^{-1}$, $N_{reps} = 1$, $m_g = 0.8 \text{ GeV}$ for several values of p^+ and N_η . For each set of parameters, three different executions of the quantum circuit are performed, for different background field configurations, consequently, each point in the plot is the mean of the three individual executions and the error bars are the respective standard deviation. The solid lines represent the analytical expectations.

4.2 Gluon

The analysis of the results for the gluon case follows closely the quark case, leading to similar conclusions. Figure 11 shows squared momentum distribution for gluon.

The impact of N_{reps} on the jet quenching parameter is shown in Figure 12, including comparison with the analytical expectation, Eq. 26. Noteworthy is that saturation scale range for which we found a good agreement with the analytical expectation is smaller than for the quark case due to more significant discrete lattice effects.

Figure 13, Figure 14, and Figure 15 show the impact of different choices of N_\perp on the jet quenching parameter. Again, the reduced range of saturation scales for which there is agreement with the analytical baseline is explained by more significant discrete lattice effects for gluons than for quarks.

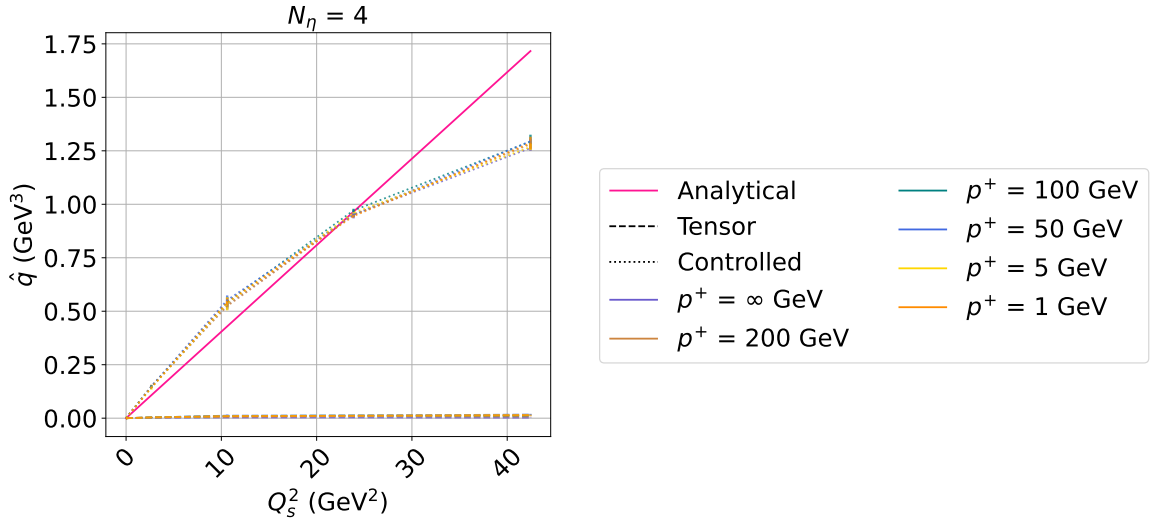


Fig. 10 Jet quenching parameter \hat{q} as a function of the saturation scale Q_s^2 for a SU(3) quark with $N_\perp = 16$, $L_\perp = 4.8 \text{ GeV}^{-1}$, $N_{\text{reps}} = 1$, $m_g = 0.8 \text{ GeV}$ for several values of p^+ and $N_\eta = 4$. For each set of parameters, three different executions of the quantum circuit are performed, for different background field configurations, consequently, each point in the plot is the mean of the three individual executions and the error bars are the respective standard deviation. The solid lines represent the analytical expectations.

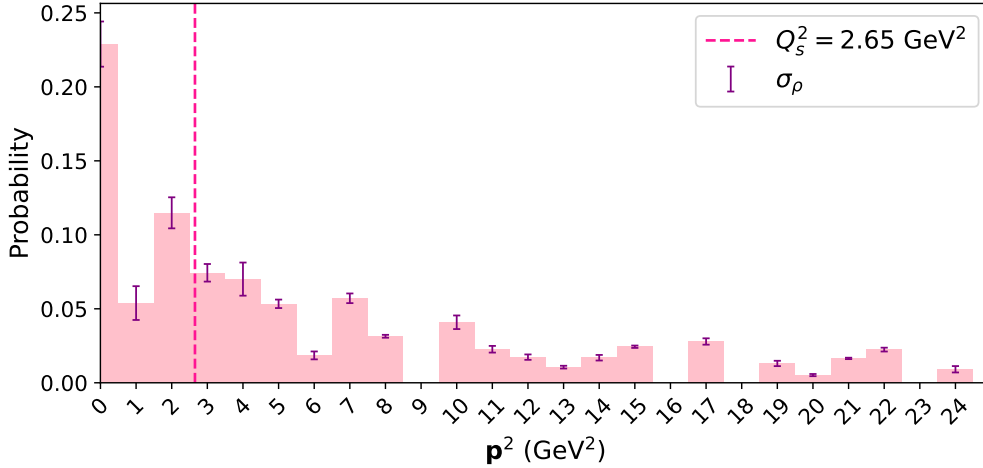


Fig. 11 Squared momentum distribution for a SU(3) gluon with $N_\perp = 8$, $L_\perp = 4.8 \text{ GeV}^{-1}$, $m_g = 0.8 \text{ GeV}$, $N_\eta = 4$, $p^+ = +\infty \text{ GeV}$, $g^2\mu = 0.5 \text{ GeV}^{\frac{3}{2}}$ and $N_{\text{reps}} = 1$. For this plot, three individual executions of the quantum circuit are presented, with the height of the bins being the mean of the three individual executions and the error bars being the respective standard deviation. Each execution corresponds to a different background field configuration. The vertical dashed line represents the saturation scale of that simulation.

5 Conclusions

This work investigated the feasibility of simulating the evolution of jets in a quantum computer, more precisely, the propagation of a single SU(3) parton through a medium. The results obtained, for both the quark and gluon cases, were analysed and compared against the classical expectation and discussed.

In a quantum simulation environment, the results closely matched analytical expectations for saturation scales below approximately 30 GeV^2 , demonstrating the potential of using quantum computers to simulate and solve this class of problems.

We found that the longitudinal evolution should be divided into as many steps as the ones of the division of the longitudinal background medium. When the longitudinal evolution is divided into more steps than the background medium ones, there is a decrease in performance. Furthermore, more divisions of the background field lead to better results, especially for smaller values of p^+ . Although some preliminary tests for SU(2) partons have shown that the controlled and tensorial methods have similar performances, for the physical meaningful theory – the SU(3) – the performance of the tensorial method vanishes.

Even though the results obtained in this work are promising, there are still many challenges to overcome. The most immediate extension of this work involves extending the Fock space to better approximate the full evolution

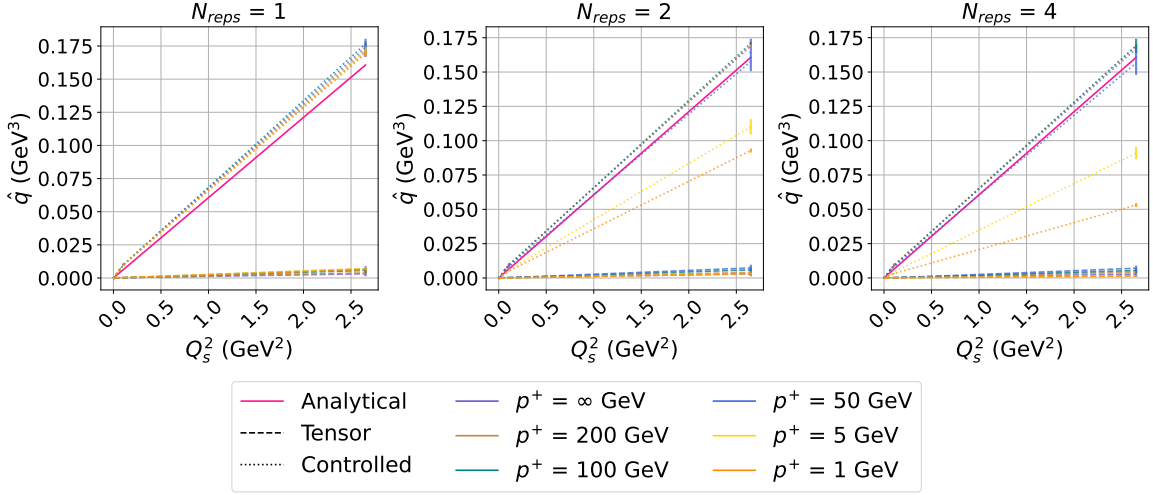


Fig. 12 Jet quenching parameter \hat{q} as a function of the saturation scale Q_s^2 for a SU(3) gluon with $N_\perp = 8$, $L_\perp = 4.8 \text{ GeV}^{-1}$, $m_g = 0.8$, $N_\eta = 16$ for several values of p^+ . For each set of parameters, three different executions of the quantum circuit are performed, for different background field configurations, consequently, each point in the plot is the mean of the three individual executions and the error bars are the respective standard deviation. The solid lines represent the analytical expectations.

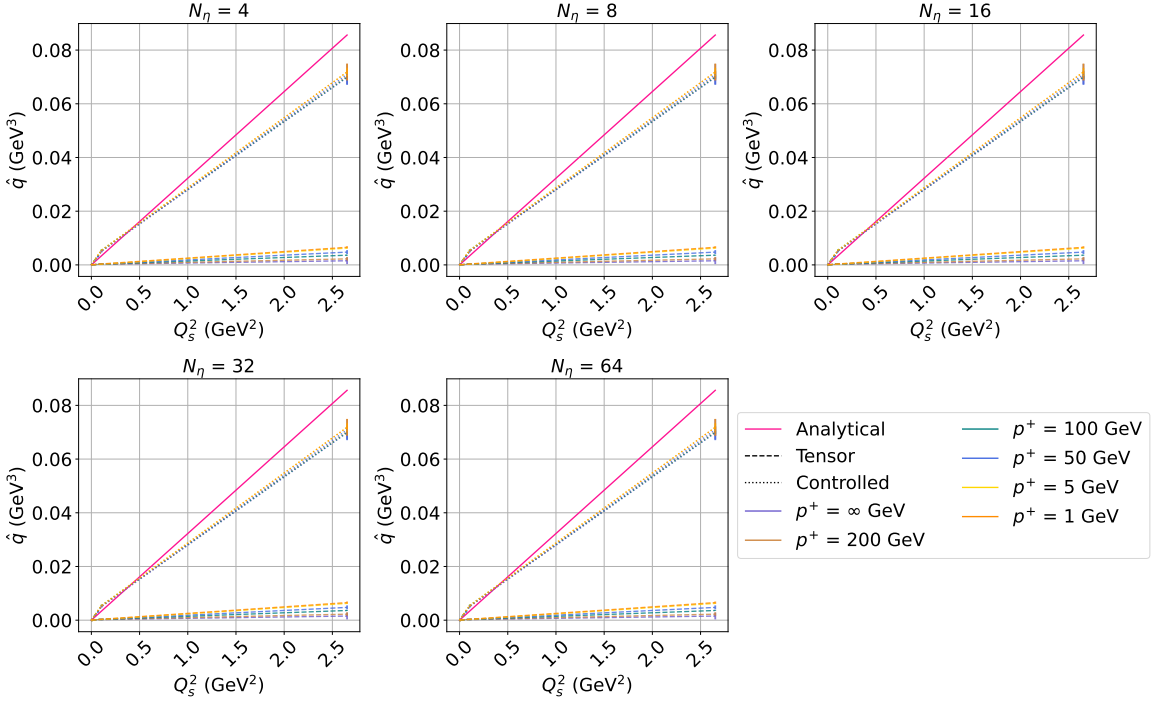


Fig. 13 Jet quenching parameter \hat{q} as a function of the saturation scale Q_s^2 for a SU(3) gluon with $N_\perp = 4$, $L_\perp = 4.8 \text{ GeV}^{-1}$, $N_{reps} = 1$, $m_g = 0.8 \text{ GeV}$ for several values of p^+ and N_η . For each set of parameters, three different executions of the quantum circuit are performed, for different background field configurations, consequently, each point in the plot is the mean of the three individual executions and the error bars are the respective standard deviation. The solid lines represent the analytical expectations.

of jets³. Another direction to follow in the future relates to the interaction with the medium. The quantum nature of the quark-gluon plasma makes the integration of the medium generation/simulation in the quantum algorithm itself a very interesting next step. Designing a procedure to simulate the entire interaction with the medium on a quantum computer would allow for a full quantum simulation of jet evolution. This full quantum regime would likely be more advantageous when fault-tolerant quantum computers become available. Furthermore, the natural representation of the SU(3) group would be a unit of information with three different states, one for each colour. From the quantum information perspective, this would involve a qutrit [22,23] or a hybrid qubit-qutrit [24] representation. Finally, the proposed algorithm is expected to be improvable by exploring quantum error mitigation techniques [25,26,27,28]. It should be remarked, nonetheless, that even if this is a promising path, it is

³Although in [18] the Fock space was already extended to include the gluon production, the simulation was performed for a very simple case with $N_\perp = 1$. Therefore, the next major step in this direction is to extend the Fock space using lattices and saturation scales similar to those employed here.

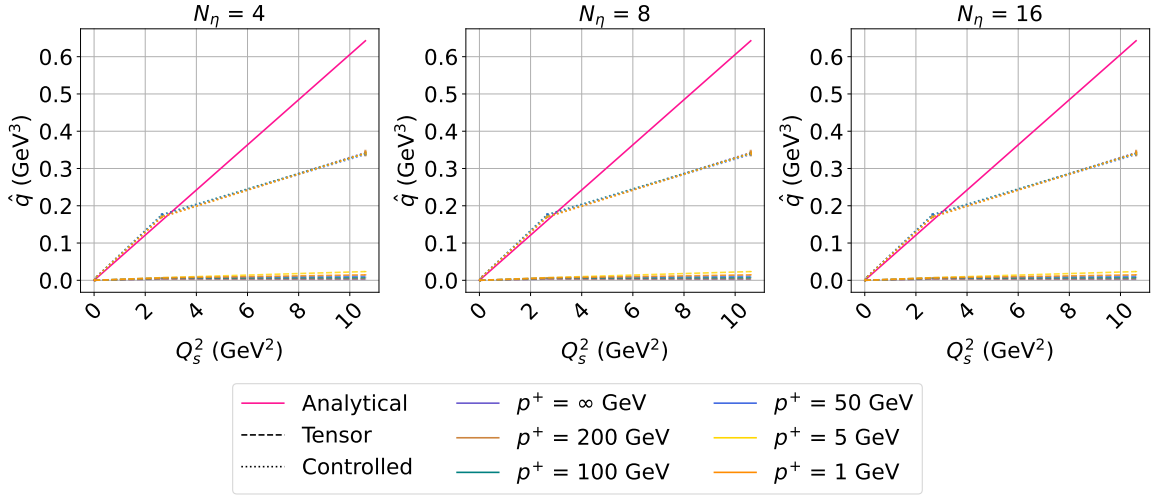


Fig. 14 Jet quenching parameter \hat{q} as a function of the saturation scale Q_s^2 for a SU(3) gluon with $N_\perp = 8$, $L_\perp = 4.8 \text{ GeV}^{-1}$, $N_{reps} = 1$, $m_g = 0.8 \text{ GeV}$ for several values of p^+ and N_η . For each set of parameters, three different executions of the quantum circuit are performed, for different background field configurations, consequently, each point in the plot is the mean of the three individual executions and the error bars are the respective standard deviation. The solid lines represent the analytical expectations.

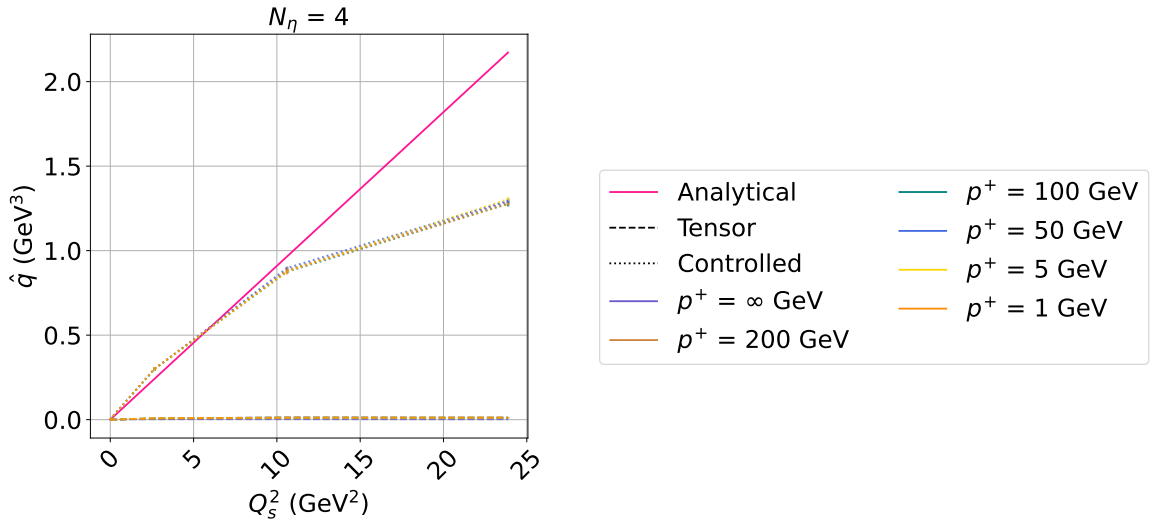


Fig. 15 Jet quenching parameter \hat{q} as a function of the saturation scale Q_s^2 for a SU(3) gluon with $N_\perp = 16$, $L_\perp = 4.8 \text{ GeV}^{-1}$, $N_{reps} = 1$, $m_g = 0.8 \text{ GeV}$ for several values of p^+ and $N_\eta = 4$. For each set of parameters, three different executions of the quantum circuit are performed, for different background field configurations, consequently, each point in the plot is the mean of the three individual executions and the error bars are the respective standard deviation. The solid lines represent the analytical expectations.

not foreseeable that such error mitigation techniques will drastically improve the current results in a near future, due to the high dimensionality of the circuits.

In conclusion, this work, along with other studies [16, 17, 18], represents one of the first steps on the long road towards simulating the full evolution of jets on a quantum computer. Even though the results demonstrate the feasibility of the quantum simulation of the jet evolution, there are still challenges to overcome and many steps to follow to achieve a full simulation of jets in a quantum computer.

Acknowledgements We would like to thank João Barata and Carlos Salgado for the relevant and interesting meetings and all the helpful information. We would also like to thank Ricardo Ribeiro and José Rufino for kindly providing access to some of the computing systems used in this work. We acknowledge the use of IBM Quantum services for this work. This work was produced with the computational support of INCN funded by FCT and FEDER under the project with reference 2023.10635.CPCA.A1. This work was financed by national funds through FCT - Fundação para a Ciência e a Tecnologia, I.P., within the scope of the project CERN/FIS- PAR/0032/2021 and by European Research Council (ERC) under the European Union's Horizon 2020 research and innovation programme (Grant agreement No. 835105, YoctoLHC).

Appendix A: colour background field

The statistics of the colour background field are described by a version of the McLerran-Venugopalan model [29, 30] that assumes that the colour charges of the medium are correlated white-noise statistics, just as assumed in

[17,18]. Hence, the colour background field is a classical stochastic field, which satisfies the reduced Yang-Mills equations,

$$\left(m_g^2 - \nabla_{\perp}^2\right) \mathcal{A}_a^-(x^+, \mathbf{x}) = \rho_a(x^+, \mathbf{x}), \quad (\text{A.1})$$

where m_g is the gluon mass, introduced to regularise the infrared divergence, ensuring the colour neutrality of the source distribution [31], and $\rho_a(x^+, \mathbf{x})$ is the colour charge density describing the medium's energetic degrees of freedom. The colour charge density is assumed to have a Gaussian correlation function, i.e.,

$$\langle\langle \rho_a(x^+, \mathbf{x}) \rho_b(x^+, \mathbf{y}) \rangle\rangle = g^2 \mu^2 \delta_{ab} \delta^{(2)}(\mathbf{x} - \mathbf{y}) \delta(x^+ - y^+), \quad (\text{A.2})$$

where $\langle\langle \dots \rangle\rangle$ denotes the average over different medium configurations, g is the QCD coupling constant, and μ has dimension of $\text{GeV}^{\frac{3}{2}}$ and can be interpreted as the medium's density of scattering centres and so determines the strength of the parton-medium interaction. In the context of high-energy scattering processes, the charge density is usually integrated over the longitudinal extension of the medium. This new quantity is known as the saturation scale Q_s^2 defined in Eq. 23.

By solving Eq. A.1, the background field can finally be expressed as

$$\mathcal{A}_a^-(x^+, \mathbf{x}) = \int d^2\mathbf{y} \frac{d^2\mathbf{k}}{(2\pi)^2} \frac{e^{-i\mathbf{k}\cdot(\mathbf{x}-\mathbf{y})}}{m_g^2 + \mathbf{k}^2} \rho_a(x^+, \mathbf{y}). \quad (\text{A.3})$$

Appendix B: Analytical jet quenching parameter

The first step to compute the analytical jet quenching parameter is to rewrite Eq. 24 as

$$\hat{q} = \frac{\langle\langle \psi_0 | U^\dagger(L_\eta; 0) \hat{\mathbf{p}}^2 U(L_\eta; 0) | \psi_0 \rangle\rangle}{L_\eta}, \quad (\text{B.4})$$

where $|\psi_0\rangle$ is the initial state of the system, and $U(L_\eta; 0)$ is the usual time evolution operator from the light-front time 0 to the light-front time L_η , i.e., for the whole medium. Through a Fourier transform, the \hat{q} in coordinate space is given by

$$\hat{q} = \frac{1}{L_\eta} \int dx dy d\mathbf{k} e^{-i\mathbf{k}\cdot(\mathbf{x}-\mathbf{y})} \mathbf{k}^2 \langle\langle \mathcal{W}^\dagger(\mathbf{y}) \mathcal{W}(\mathbf{x}) \rangle\rangle = \frac{1}{L_\eta} \int d\mathbf{x} \langle\langle \nabla_{\mathbf{y}} \mathcal{W}^\dagger(\mathbf{y}) \cdot \nabla_{\mathbf{x}} \mathcal{W}(\mathbf{x}) \rangle\rangle, \quad (\text{B.5})$$

where $\nabla_{\mathbf{k}}$ is the directional derivative along \mathbf{k} , and \mathcal{W} is a Wilson line along x^+ in the light-cone framework which can be explicitly written as

$$\mathcal{W}(\mathbf{x}) = e^{-ig \int_0^{L_\eta} dx^+ \mathcal{A}^-(x^+, \mathbf{x})}, \quad (\text{B.6})$$

and corresponds to the evolution operator (Eq. 6) in the eikonal limit, i.e., $p^+ \rightarrow \infty$ ⁴. For the quark case, the above Wilson line should be used in the fundamental form, i.e., $\mathcal{A}^-(x^+, \mathbf{x})$ should be replaced by $\mathcal{A}_a^-(x^+, \mathbf{x}) \mathbf{t}^a$, and for the gluon case, the adjoint form, i.e., replaced by $\mathcal{A}_a^-(x^+, \mathbf{x}) \mathbf{T}'^a$.

By choosing coincident coordinates $\mathbf{y} = \mathbf{x}$, and substituting the Wilson line (Eq. B.6) in the expression for \hat{q} , one obtains

$$\begin{aligned} \hat{q} &= \frac{1}{L_\eta} \langle\langle \nabla_{\mathbf{y}} \mathcal{W}^\dagger(\mathbf{y}) \cdot \nabla_{\mathbf{x}} \mathcal{W}(\mathbf{x}) \rangle\rangle_{\mathbf{y}=\mathbf{x}} \\ &= \frac{1}{L_\eta} \langle\langle \nabla_{\mathbf{y}} e^{ig \int_0^{L_\eta} dy^+ \mathcal{A}^-(y^+, \mathbf{y})} \cdot \nabla_{\mathbf{x}} e^{-ig \int_0^{L_\eta} dx^+ \mathcal{A}^-(x^+, \mathbf{x})} \rangle\rangle_{\mathbf{y}=\mathbf{x}} \\ &= \frac{g^2}{L_\eta} \int_0^{L_\eta} dx^+ \int_0^{L_\eta} dy^+ \cdot \langle\langle \nabla_{\mathbf{y}} \mathcal{A}_a^-(y^+, \mathbf{y}) t^a \cdot \nabla_{\mathbf{x}} \mathcal{A}_b^-(x^+, \mathbf{x}) t^b \rangle\rangle_{\mathbf{y}=\mathbf{x}}. \end{aligned} \quad (\text{B.7})$$

In Eq. B.6, the Wilson line is explicitly written in the fundamental form for the quark case, and, if one wants to analyze the gluon case, one should replace the fundamental matrices with the adjoint ones. Now, by using the background field definition (Eq. A.3) and by omitting the colour indices for simplicity, the \hat{q} for a quark can be rewritten as

⁴In [32] is shown that assuming finite p^+ values, and so, including the kinetic term at the leading eikonal order, does not affect the \hat{q} .

$$\begin{aligned}
\hat{q} &= \frac{g^2}{L_\eta} \int_0^{L_\eta} dx^+ \int_0^{L_\eta} dy^+ \\
&\quad \langle \langle \nabla_{\mathbf{y}} \left(\int d\mathbf{z} \frac{d^2 \mathbf{k}}{(2\pi)^2} \frac{e^{i\mathbf{k}(\mathbf{y}-\mathbf{z})}}{m_g^2 + \mathbf{k}^2} \rho(y^+, \mathbf{z}) t \right) \cdot \nabla_{\mathbf{x}} \left(\int d\mathbf{w} \frac{d^2 \mathbf{l}}{(2\pi)^2} \frac{e^{-i\mathbf{l}(\mathbf{x}-\mathbf{w})}}{m_g^2 + \mathbf{l}^2} \rho(x^+, \mathbf{w}) t \right) \rangle \rangle_{\mathbf{y}=\mathbf{x}} \\
&= \frac{g^2}{L_\eta} \int_0^{L_\eta} dx^+ \int_0^{L_\eta} dy^+ \int d\mathbf{z} \frac{d^2 \mathbf{k}}{(2\pi)^2} \\
&\quad \cdot \mathbf{k} \frac{e^{i\mathbf{k}(\mathbf{x}-\mathbf{z})}}{m_g^2 + \mathbf{k}^2} \cdot \int d\mathbf{w} \frac{d^2 \mathbf{l}}{(2\pi)^2} \mathbf{l} \frac{e^{-i\mathbf{l}(\mathbf{x}-\mathbf{w})}}{m_g^2 + \mathbf{l}^2} \langle \langle \rho(x^+, \mathbf{z}) \rho(y^+, \mathbf{w}) \rangle \rangle t \cdot t. \quad (\text{B.8})
\end{aligned}$$

Now, remembering the colour charge density correlator (Eq. A.2), one can write

$$\begin{aligned}
\langle \langle \rho(x^+, \mathbf{z}) \rho(y^+, \mathbf{w}) \rangle \rangle t \cdot t &\equiv \sum_a \sum_b \langle \langle \rho_a(x^+, \mathbf{z}) \rho_b(y^+, \mathbf{w}) \rangle \rangle t^a \cdot t^b \\
&= \sum_a \sum_b g^2 \mu^2 \delta_{ab} \delta(x^+ - y^+) \delta(\mathbf{z} - \mathbf{w}) C_F \hat{I}. \quad (\text{B.9})
\end{aligned}$$

For the gluon case, the \mathbf{t} matrices should be replaced by the \mathbf{T}' matrices, i.e.,

$$\langle \langle \rho(x^+, \mathbf{z}) \rho(y^+, \mathbf{w}) \rangle \rangle \mathbf{T}' \cdot \mathbf{T}' \equiv \sum_a \sum_b g^2 \mu^2 \delta_{ab} \delta(x^+ - y^+) \delta(\mathbf{z} - \mathbf{w}) C_A \hat{I}. \quad (\text{B.10})$$

Finally, including the result in Eq. B.9 in the expression for \hat{q} , one obtains

$$\begin{aligned}
\hat{q} &= \frac{g^2}{L_\eta} g^2 \mu^2 C_F \int_0^{L_\eta} dx^+ \int d\mathbf{z} \frac{d^2 \mathbf{k}}{(2\pi)^2} \mathbf{k} \frac{e^{i\mathbf{k}(\mathbf{x}-\mathbf{z})}}{m_g^2 + \mathbf{k}^2} \int \frac{d^2 \mathbf{l}}{(2\pi)^2} \mathbf{l} \frac{e^{-i\mathbf{l}(\mathbf{x}-\mathbf{z})}}{m_g^2 + \mathbf{l}^2} \\
&= g^4 \mu^2 C_F \int \frac{d^2 \mathbf{p}_\perp}{(2\pi)^2} \frac{\mathbf{p}_\perp^2}{(m_g^2 + \mathbf{p}_\perp^2)^2} \quad (\text{B.11})
\end{aligned}$$

The discrete nature of the transverse lattice introduces two momentum cutoffs, which are the Infra-Red (IR) and the Ultra-violet (UV) cutoffs, and which are defined as $\lambda_{IR} = \frac{\pi}{L_\perp}$ and $\lambda_{UV} = \frac{\pi}{\Delta_\perp} = \lambda_{IR} N_\perp$, respectively. Thus, the above integral can be rewritten in polar coordinates, with p the module of \mathbf{p}_\perp , as

$$\begin{aligned}
\hat{q} &= g^4 \mu^2 C_F \int_{\lambda_{IR}}^{\lambda_{UV}} dp \int_0^{2\pi} \frac{d\theta}{(2\pi)^2} p \frac{p^2}{(m_g^2 + p^2)^2} \\
&= g^4 \mu^2 C_F \int_{\lambda_{IR}}^{\lambda_{UV}} \frac{dp}{2\pi} \frac{p^3}{(m_g^2 + p^2)^2} \quad (\text{B.12}) \\
&= \frac{g^4 \mu^2 C_F}{4\pi} \left(\log \left(\frac{1 + \frac{\Delta_\perp^2 m_g^2}{\pi^2}}{\frac{1}{N_\perp^2} + \frac{\Delta_\perp^2 m_g^2}{\pi^2}} \right) - \frac{\Delta_\perp^2 m_g^2}{\pi^2} \left(\frac{1}{\frac{1}{N_\perp^2} + \frac{\Delta_\perp^2 m_g^2}{\pi^2}} - \frac{1}{1 + \frac{\Delta_\perp^2 m_g^2}{\pi^2}} \right) \right).
\end{aligned}$$

From Eq. B.9 and Eq. B.10, one can trivially see that when the propagating parton is a gluon instead of a quark, the factor C_F should be replaced by C_A .

References

1. G.P. Salam, *The European Physical Journal C* **67**(3–4), 637–686 (2010). DOI 10.1140/epjc/s10052-010-1314-6
2. U.A. Wiedemann, *Jet Quenching in Heavy Ion Collisions* (Springer Berlin Heidelberg, 2010), p. 521–562. DOI 10.1007/978-3-642-01539-7_17. URL http://dx.doi.org/10.1007/978-3-642-01539-7_17
3. A. Majumder, M. van Leeuwen, *Progress in Particle and Nuclear Physics* **66**(1), 41–92 (2011). DOI 10.1016/j.pnnp.2010.09.001. URL <http://dx.doi.org/10.1016/j.pnnp.2010.09.001>
4. Y. Mehtar-Tani, J.G. Milhano, K. Tywoniuk, *International Journal of Modern Physics A* **28**(11), 1340013 (2013). DOI 10.1142/s0217751x13400137
5. J.P. Blaizot, Y. Mehtar-Tani, *International Journal of Modern Physics E* **24**(11), 1530012 (2015). DOI 10.1142/s021830131530012x
6. G.Y. Qin, X.N. Wang, *International Journal of Modern Physics E* **24**(11), 1530014 (2015). DOI 10.1142/s0218301315300143. URL <http://dx.doi.org/10.1142/S0218301315300143>
7. L. Apolinário, Y.J. Lee, M. Winn, *Progress in Particle and Nuclear Physics* **127**, 103990 (2022). DOI 10.1016/j.pnnp.2022.103990. URL <http://dx.doi.org/10.1016/j.pnnp.2022.103990>
8. I.P. Lokhtin, A.M. Snigirev, *Journal of Physics G: Nuclear and Particle Physics* **34**(8), S999–S1003 (2007). DOI 10.1088/0954-3889/34/8/s143
9. N. Armesto, L. Cunqueiro, C.A. Salgado, *Eur. Phys. J. C* **63**, 679 (2009). DOI 10.1140/epjc/s10052-009-1133-9
10. K. Zapp, *The European Physical Journal C* **74**(2) (2014). DOI 10.1140/epjc/s10052-014-2762-1

11. J. Casalderrey-Solana, D.C. Gulhan, J.G. Milhano, D. Pablos, K. Rajagopal, *Journal of High Energy Physics* **2014**(10) (2014). DOI 10.1007/jhep10(2014)019
12. J.H.P. et al. The jetscape framework (2019)
13. S.J. Freedman, J.F. Clauser, *Phys. Rev. Lett.* **28**, 938 (1972). DOI 10.1103/PhysRevLett.28.938
14. A. Aspect, J. Dalibard, G. Roger, *Phys. Rev. Lett.* **49**, 1804 (1982). DOI 10.1103/PhysRevLett.49.1804
15. J. Preskill, *Quantum* **2**, 79 (2018). DOI 10.22331/q-2018-08-06-79
16. J. Barata, C. Salgado, *The European Physical Journal C* **81** (2021). DOI 10.1140/epjc/s10052-021-09674-9
17. J. Barata, X. Du, M. Li, W. Qian, C.A. Salgado, *Phys. Rev. D* **106**, 074013 (2022). DOI 10.1103/PhysRevD.106.074013
18. J. Barata, X. Du, M. Li, W. Qian, C.A. Salgado, *Phys. Rev. D* **108**, 056023 (2023). DOI 10.1103/PhysRevD.108.056023
19. M.A. Nielsen, I.L. Chuang, *Quantum Computation and Quantum Information: 10th Anniversary Edition* (Cambridge University Press, 2011)
20. Qiskit Community. Qiskit: An open-source framework for quantum computing (2017). DOI 10.5281/zenodo.2562110. URL <https://github.com/Qiskit/qiskit>
21. E. Iancu, P. Taels, B. Wu, *Physics Letters B* **786**, 288 (2018). DOI 10.1016/j.physletb.2018.10.007
22. P. Gokhale, J.M. Baker, C. Duckering, F.T. Chong, N.C. Brown, K.R. Brown, *IEEE Micro* **40**, 64 (2020). DOI 10.1109/MM.2020.2985976
23. T. Roy, Z. Li, E. Kapit, D.I. Schuster, *Phys. Rev. Appl.* **19**, 064024 (2023). DOI 10.1103/PhysRevApplied.19.064024
24. T. Bækkegaard, L.B. Kristensen, N.J.S. Loft, C.K. Andersen, D. Petrosyan, N.T. Zinner, *Scientific Reports* **9**(1) (2019). DOI 10.1038/s41598-019-49657-1
25. Z. Cai, R. Babbush, S.C. Benjamin, S. Endo, W.J. Huggins, Y. Li, J.R. McClean, T.E. O'Brien, *Rev. Mod. Phys.* **95**, 045005 (2023). DOI 10.1103/RevModPhys.95.045005
26. K. Temme, S. Bravyi, J.M. Gambetta, *Phys. Rev. Lett.* **119**, 180509 (2017). DOI 10.1103/PhysRevLett.119.180509
27. E. van den Berg, Z.K. Mineev, A. Kandala, K. Temme, *Nature Physics* **19**(8), 1116–1121 (2023). DOI 10.1038/s41567-023-02042-2
28. J.J. Wallman, J. Emerson, *Physical Review A* **94**(5) (2016). DOI 10.1103/physreva.94.052325
29. L. McLerran, R. Venugopalan, *Physical Review D* **49**(7), 3352 (1994). DOI 10.1103/physrevd.49.3352
30. L. McLerran, R. Venugopalan, *Physical Review D* **49**(5), 2233 (1994). DOI 10.1103/physrevd.49.2233
31. A. Krasnitz, Y. Nara, R. Venugopalan, *Nuclear Physics A* **717**(3), 268 (2003). DOI [https://doi.org/10.1016/S0375-9474\(03\)00636-5](https://doi.org/10.1016/S0375-9474(03)00636-5)
32. J. Blaizot, F. Dominguez, E. Iancu, Y. Mehtar-Tani, *Journal of High Energy Physics* **2013**(1) (2013). DOI 10.1007/jhep01(2013)143